International Journal of Heat and Mass Transfer 218 (2024) 124765

Contents lists available at ScienceDirect

International Journal of Heat and Mass Transfer

journal homepage: www.elsevier.com/locate/ijhmt

Influences of laser heating parameters on thermophoretic enrichment of nanoparticles

Jing Dong [a], Dongfang Liang [a,*], Xinan Chen [b], Xin Yang [c]

[a] Department of Engineering, University of Cambridge, Cambridge CB2 1PZ, UK
[b] School of Computer Science, University of Nottingham, Nottingham NG72RD, UK
[c] Department of Electrical and Electronic Engineering, School of Engineering, Cardiff University, Cardiff CF24 3AA, UK

ARTICLE INFO

Keywords:
Nanoparticles
Thermophoresis
Laser
Microfluidics

ABSTRACT

Thermophoretic enrichment of particles has been recognised as an efficient way to concentrate nanovesicles in biomedical studies. Although some experimental and analytical studies have been undertaken to examine the thermophoretic accumulation mechanisms, few studies have been conducted to optimise the device design. This paper presents a detailed parametric study of a thermophoretic enrichment system, which sandwiches a microchamber containing particle/fluid mixture by a glass top, from where an infrared laser heat source is introduced, and a sapphire bottom, which has a high heat conductivity to prevent overheating. The influences of the laser spot radius, laser attenuation rate, nanoparticle size and laser power are investigated. The radius of the nanoparticle accumulation zone is found to be approximately 1.25 times the laser spot radius. A reduction in the laser attenuation length leads to a reduction of the time taken by the nanoparticles to reach the steady state, but an enlarged zone over which nanoparticles are concentrated. There exists an optimum range of the attenuation length, depending on the required size of the target area. We have also determined the threshold particle size, which decides whether the particle motion is convection-dominated or thermophoresis-dominated. Furthermore, an increase in the laser power reduces the accumulation time. These findings provide guidelines for the design of enrichment systems.

1. Introduction

Nanovesicles such as exosomes, of 30–150 nm in diameter, and microvesicles (MVs), of 200–1,000 nm in diameter, have attracted increasing attention, as they provide an unbiased and global readout of tumours [1]. However, technical constraints prevent them from being fully leveraged as the new liquid biopsy paradigm for early cancer detection. Most available diagnostic tests for nanovesicles suffer from low sensitivity, poor efficiency and large sample consumption. For example, ultracentrifugation is the most commonly used technique in exosome separation and concentration, but it is of low purity, low yield, and low efficiency [2]. Such limitations restrict their applications to clinical testing, which involves serial analyses, large patient cohorts and limited specimens. Recent advances in lab-on-a-chip technologies have led to the innovation of portable microfluidic devices for microparticle separation and concentration, employing various physical mechanisms such as centrifugation [3,4], inertia-driven flow [5], dielectrophoresis [6], optical trapping [7] and acoustophoresis [8,9]. However, these approaches are ineffective for nanoparticle processing due to the steep decrease of the body forces generated by them as the particle size decreases and the strong Brownian motion of submicron- and nanometre-sized species. Recently, thermophoresis has been proposed as an effective strategy for the manipulation of nanoparticles due to its fast, low-cost and easy-to-operate characteristics [10,11].

Ludwig is the first to describe the phenomenon of thermophoresis [12]. Thermophoresis, also called thermal migration, replies on the effect of the temperature gradient on particles, which drives them to move from a hot region to a cold region [13,14]. This phenomenon is an additional transport mechanism complementary to molecular diffusion. The Soret (S_T) coefficient is the magnitude that represents this migration, and it is the ratio between the thermal diffusion (D_T) and material diffusion (D) coefficients, $S_T = D_T/D$. The total mass flux can be written as follows [15]

$$J = -D\nabla c - cD_T\nabla T \tag{1}$$

* Corresponding author.
E-mail address: dl359@cam.ac.uk (D. Liang).

https://doi.org/10.1016/j.ijheatmasstransfer.2023.124765
Received 29 July 2023; Received in revised form 12 September 2023; Accepted 26 September 2023
Available online 6 October 2023

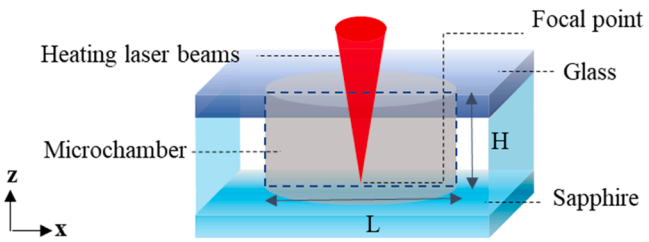

Fig. 1. Schematic of the thermophoretic enrichment model setup.

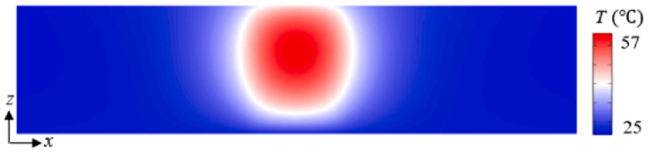

Fig. 2. Temperature field in the middle section.

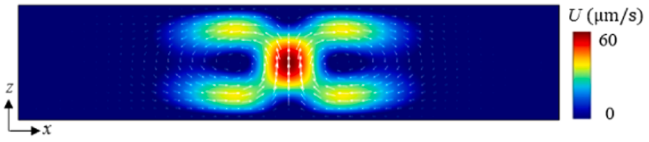

Fig. 3. Velocity field in the middle section.

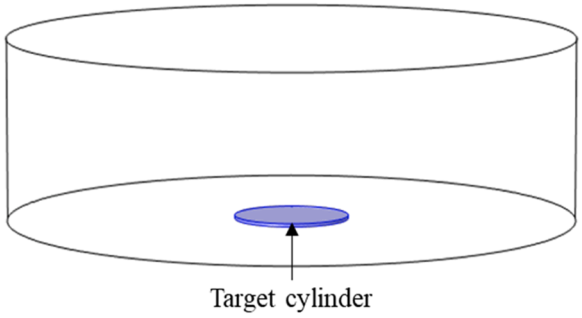

Fig. 4. Schematic of target cylinder centred at the final positions of nanoparticles.

where J is the net mass flux, c is the concentration, and ∇T is the temperature gradient.

In a typical thermophoresis enrichment system, an infrared (IR) laser beam is introduced into the particle/fluid mixture in a microchamber to induce the temperature variation [16]. The liquid around the centre of the microchamber experiences the maximum temperature. The local heating drives a toroidal convective flow that continuously pushes particles toward the centre of the chamber at the bottom. Meanwhile, thermophoresis tends to repel particles away from the hot liquid core, preventing particles rising up and thus leading to particle accumulation at the centre of the chamber bottom. There have been some experimental studies demonstrating nanoparticle enrichment using thermophoretic effects. Liu et al. first utilised the principle of thermophoresis to establish a thermophoretic aptamer platform for the accumulation of EVs [10]. Both exosomes (30 – 150 nm) and microvesicles (200 – 1,000 nm) can be effectively accumulated by thermophoresis within 10 mins. Tian et al. used a thermophoretic aptasensor to profile cancer-associated protein markers from plasma EVs and predicted the course of metastatic breast cancer [11]. Recently, Huang et al. developed a newly evolved aptamer with rapid binding kinetics that can efficiently bind to PD-L1. Meanwhile, the strong thermophoretic effect of high-charge aptamers has been utilised to establish a simple, fast, separation-free and homogeneous thermophoresis EV enrichment approach for EV PD-L1 sensitive quantification [17]. Thermophoresis has also been employed to concentrate nucleic acids (DNAs and RNAs), according to their comprehensive length or stem configuration [18].

No research has conducted on the influence of the laser parameters on the nanoparticle thermophoretic enrichment. These parameters change the temperature field and are thus expected to play important roles in the particle enrichment process, affecting both the final particle positions and the particle accumulation time. Our research systematically investigates key laser parameters, including the laser spot radius, the laser attenuation rate, and the laser power. The spot radius of the laser determines the size of the heating core in the middle of the microchamber. The attenuation length of the laser influences the accumulation efficiency by changing the gap between the heating core and the bottom of the chamber. In addition, the influence of the laser power on the accumulation efficiency is not well understood and thus is also investigated. Our findings offer a comprehensive understanding of these factors' impact on nanoparticle accumulation, thereby providing insights into the optimal design of the laser system for efficient thermophoretic enrichment. Another key part of our research focuses on identifying the threshold particle size for successful enrichment. Such information contributes to ascertain the dominant mechanism that governs the particle motion, revealing the limit of thermophoretic enrichment. In this work, the finite element method is used to numerically model the thermophoresis enrichment. The liquid motion is governed by the continuity and Navier-Stokes equations. The thermophoretic force, drag force, lift force, Brownian force and buoyancy act on solid particles to drive their motion. To validate this numerical model, a past case study published by Liu et al. is reproduced [10] by the current model. After studying the sensitivity to the microchamber height, we used our model to investigate the influence of the spot radius of the laser, the light attenuation length and the laser power on the nanoparticle enrichment efficiency.

2. Governing equations

The Eulerian-Lagrangian approach is used in this study. The liquid is considered a continuous phase using the Eulerian description, while the suspended particles dispersed in the liquid are tracked employing the Lagrangian description [19,20]. The finite element method (FEM) is implemented to simulate heat transfer, laminar flow, and particle motion.

In all cases, flat-top IR laser beams are used in the experiments,

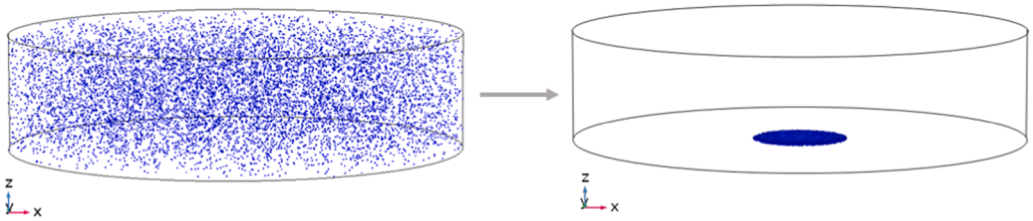

Fig. 5. Simulation of particle accumulation of EVs.

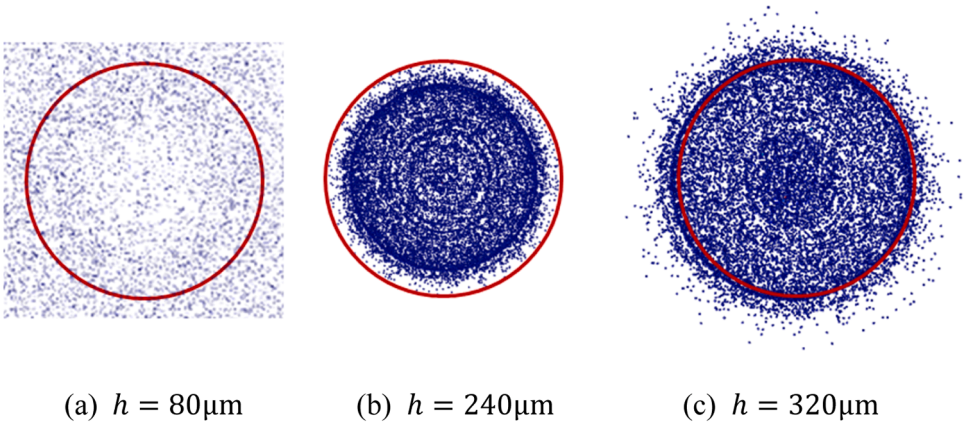

Fig. 6. Top view of target cylinder at the steady state for different chamber heights.

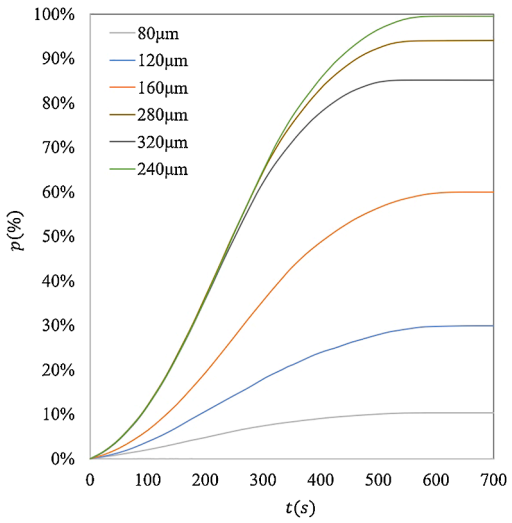

Fig. 7. Percentages of particles in the target cylinder for selected chamber heights.

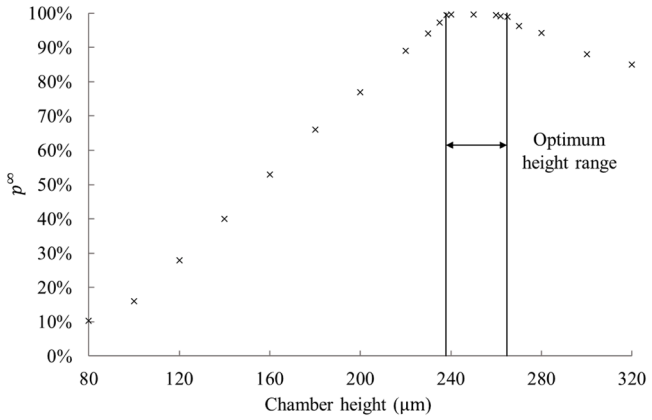

Fig. 8. Final percentages of particles in the target cylinder for all tested chamber heights.

serving as the heat source [10]. The power density is constant horizontally within the working area, whose radius is r_0, while it attenuates along the vertical direction. For flat-top beams, the laser power outside the working area is zero. The power density distribution of the IR laser in working area is modelled according to the Beer-Lambert law [21]:

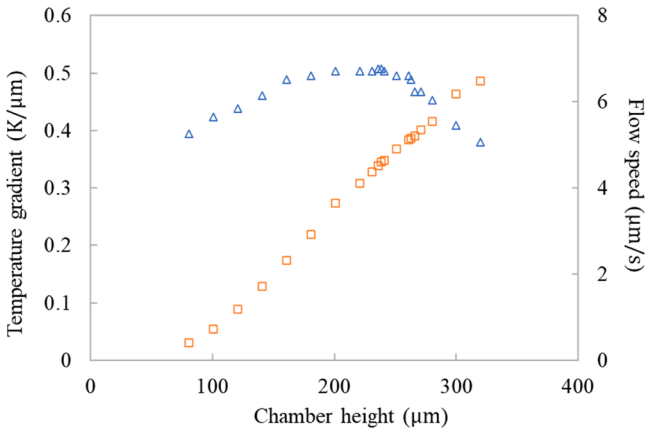

Fig. 9. Temperature gradients (blue) and convection flow speeds (orange) at 5 μm above the centre of the microchamber bottom for different heights.

$$Q = Q_0/(\pi r_0^2) \times \exp(-(H-z)/\lambda) \tag{2}$$

where Q is the power density function in the liquid, Q_0 is the total laser power, r_0 is the spot radius of the laser, H is the height of the microchamber, z is the vertical coordinate, and λ is the attenuation length.

The motion of an incompressible fluid is governed by the conservation of mass and momentum [22]:

$$\nabla\cdot(\rho \boldsymbol{v}) = 0 \tag{3}$$

$$\frac{\partial(\rho \boldsymbol{v})}{\partial t} + \nabla\cdot(\rho \boldsymbol{v}\boldsymbol{v}) = -\nabla p + \nabla\cdot(\mu\nabla \boldsymbol{v}) - \rho\alpha(T - T_0)\boldsymbol{g} \tag{4}$$

where ρ is the fluid density, μ is the dynamic viscosity of the fluid, $\boldsymbol{v}$ is the velocity vector, p is pressure, α is the thermal expansion coefficient of the fluid, $\boldsymbol{g}$ is gravitational acceleration vector, T is the warm fluid temperature, and T_0 is the ambient temperature. The Boussinesq approximation is employed to model natural convection.

The conservation of energy can be expressed by [23]:

$$\rho c_p \frac{\partial T}{\partial t} + \rho c_p \boldsymbol{v}\cdot\nabla T = \nabla\cdot(k\nabla T) + \mathrm{Q} \tag{5}$$

where c_p is the heat capacity and k is the thermal conductivity of the fluid.

The forces acting on the nanoparticles include the thermophoretic force, the drag force, the lift force, the Brownian force and the buoyancy force. The particle-particle interactions are not considered since the particle volume fraction is relatively small. The motion of a particle can

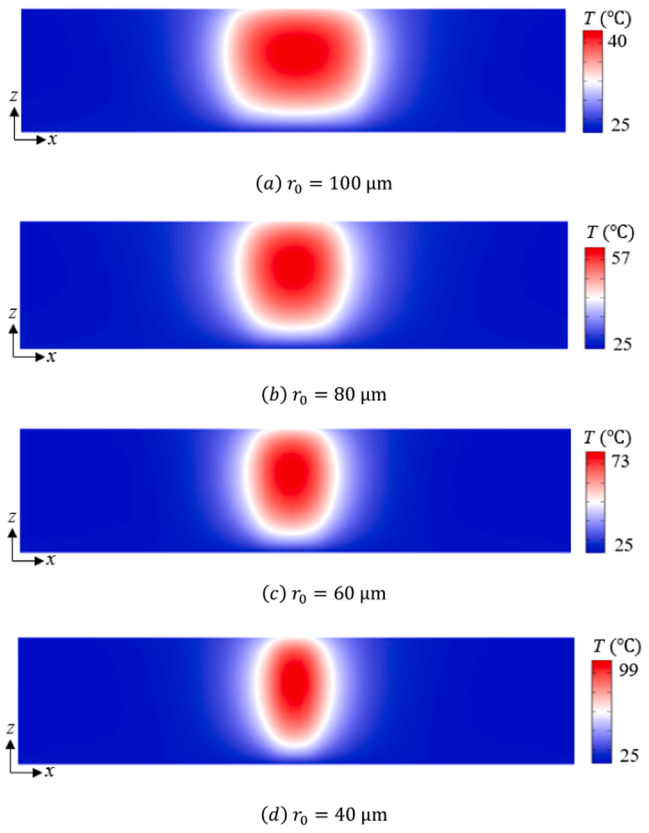

Fig. 10. Temperature fields for different r_0 values.

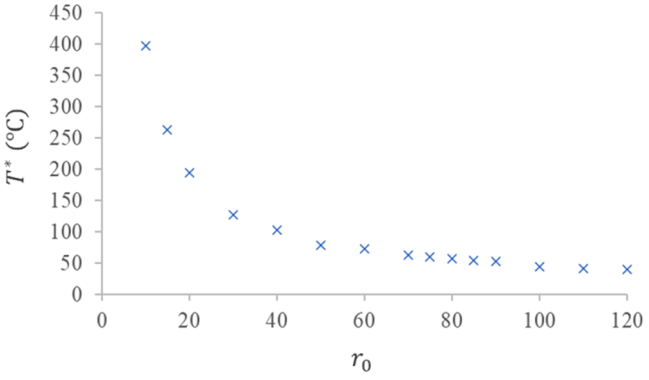

Fig. 11. Maximum temperatures (T^*) for different r_0 values.

be described by [24–28]:

$$\frac{d\boldsymbol{v}_p}{dt} = \boldsymbol{F}_D + \boldsymbol{F}_T + \boldsymbol{F}_b + \boldsymbol{F}_l + \boldsymbol{g}\left(\frac{\rho_p - \rho}{\rho_p}\right) \tag{6}$$

where $\boldsymbol{v}_p$ is the velocity of the particle, $\boldsymbol{F}_D$ is the drag force per unit particle mass, $\boldsymbol{F}_T$ is the thermophoretic force per unit particle mass, $\boldsymbol{F}_b$ is the Brownian force per unit particle mass, $\boldsymbol{F}_l$ is the Saffman's lift force per unit particle mass due to shearing, and ρ_p is the particle density.

The drag force is defined as [29]:

$$\boldsymbol{F}_D = \frac{1}{\tau_p}\left(\boldsymbol{v} - \boldsymbol{v}_p\right) \tag{7a}$$

where τ_p is the particle velocity response time. Here, the relative Reynolds number of the particles in the fluid is very small, so the Stokes drag law is applicable. According to the Stokes drag law, the velocity response time is defined as:

$$\tau_p = \frac{\rho_p d_p^2}{18\mu} \tag{7b}$$

where d_p is the particle diameter.

The thermophoretic force is used to model the thermophoresis phenomenon, which causes particles to migrate in a fluid with a nonuniform temperature field. It is expressed by [25]:

$$\boldsymbol{F}_T = \frac{6\pi\mu r_p \boldsymbol{v}}{m_p} = \frac{-6\pi\mu r_p D_T \nabla T}{m_p} = \frac{-6\pi\mu r_p S_T D \nabla T}{m_p} \tag{8}$$

where r_p is the particle radius, and m_p is the particle mass.

The Brownian force is modelled as a Gaussian white noise random process given by [30]:

$$\boldsymbol{F}_b = \boldsymbol{\zeta}\sqrt{\frac{\pi G_0}{\Delta t}} \text{ and } G_0 = \frac{216 k_B \mu T}{\pi^2 d_p^5 \rho_p^2 C_c} \tag{9}$$

where Δt is the time step adopted by the solver, $k_B = 1.380649 \times 10^{-23}$ J/K is the Boltzmann constant, C_c is the Stokes-Cunningham slip correction, and $\boldsymbol{\zeta}$ represents a vector whose components are independent random numbers obeying a normal distribution with zero mean and unit variance [31].

Moreover, submicron particles in a shear flow field experience a lift force perpendicular to the direction of the flow. This shear lift originates from the inertia effects in the viscous flow around the particle. For small-Reynolds-number flows, it can be estimated by Eq. (10) [32].

$$\boldsymbol{F}_l = \frac{2\mathrm{K}(\mu/\rho)^{1/2}\rho \boldsymbol{d}_{ij}}{\rho_p d_p (\boldsymbol{d}_{lk}\boldsymbol{d}_{kl})^{1/4}} \cdot \left(\boldsymbol{v} - \boldsymbol{v}_p\right) \tag{10}$$

where K=2.594, and $\boldsymbol{d}_{ij}$ is the fluid deformation rate tensor.

3. Numerical model

Fig. 1 presents a 3D view of the thermophoretic enrichment system for accumulating nanoparticles. The entire system is made of three parts: a glass top slide, a microchamber in the middle, and a sapphire bottom slide. L represents the diameter, and H represents the height of the microchamber. Due to the high thermal conductivity of the sapphire bottom slide, the chamber bottom experiences little temperature rise so that live nanoparticles will not suffer from thermal degradation when they accumulate on the chamber bottom. In the experiment, Polystyrene (PS) nanoparticles are diluted in water and randomly seeded in the microchamber. To generate the temperature gradient, an IR laser with a wavelength of 1, 480 nm and a power $Q_0 = 194$ mW is used [10]. The laser is a flat top beam that focuses onto the bottom of the microchamber. The accumulation of nanoparticles relies on the interplay of thermophoresis, diffusion and convection induced by localised laser heating. We aim to accumulate nanoparticles in the middle area on the bottom of the chamber.

The 3D geometry is symmetric about the z axis and can be converted to a 2D axisymmetric model, which significantly reduces the computational time and memory required to solve the partial differential equations. In all the case studies, the room temperature is taken to be T =25°C. At this temperature, the key properties of water are $\rho_0 = 997$ kg/m^3, $\mu = 0.890$ mPa·s, and the values of the density of polystyrene is $\rho_p = 1050$ kg/m^3. The thermal conductivities k of water, glass and sapphire are 0.6, 1.3 and 35 W m^{-1}K^{-1}, respectively. The heat capacities c_p of water, glass and sapphire are 4,200, 761 and 755 J Kg^{-1}K^{-1}, respectively [10].

The FEM simulation is implemented in the following procedure. First, the Laminar Flow Physics Interface and the Heat Transfer in Fluids Interface are coupled to calculate the flow field and temperature distribution by solving the Navier-Stokes equation, the continuity equation,

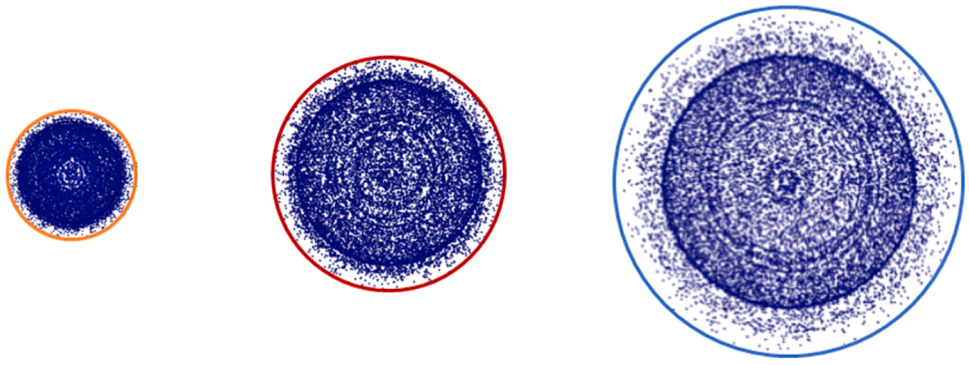

(a) $r_0 = 40$ μm (b) $r_0 = 80$ μm (c) $r_0 = 120$ μm

Fig. 12. Top view of target cylinder at the steady state for different r_0 values ($r = 3500$ μm).

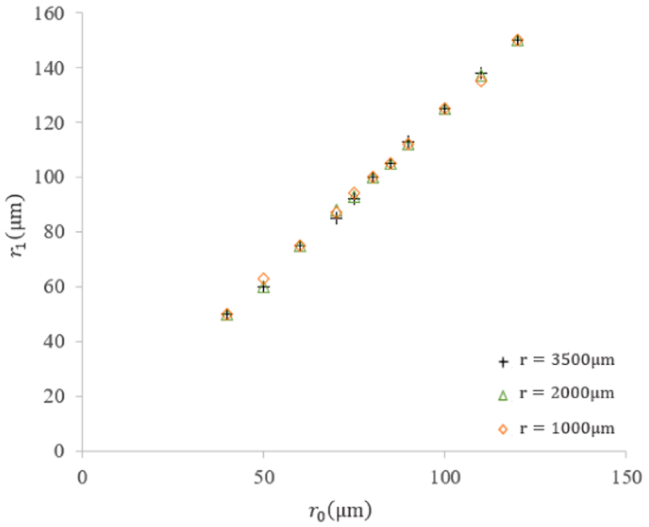

Fig. 13. Relationship between r_0 and r_1 at the steady state for all tested r_0 values.

and the energy conservation equation. In this step, the flow velocity v and temperature distribution T are determined. Then, the Particle Tracing for Fluid Flow Interface is used to calculate the thermophoretic force, the drag force, the lift force, the Brownian force and the buoyancy force acting on nanoparticles, and to determine the velocity and displacement of nanoparticles.

4. Model verifications and sensitivity to microchamber height

4.1. Verifications of model

In the first case study, extracellular vesicles (EVs) enrichment is simulated to determine the correctness of our thermophoresis model by comparing the results with those published in Liu et al. [10]. A thermophoretic aptasensor (TAS) is used to enrich EVs accumulated in the middle area on the bottom of the chamber after 10 min of laser irradiation. The mechanism of accumulation of EVs results from the interaction of thermophoresis and convection generated by localized laser heating. The radius of the laser focused spot is $r_0 = 80$ μm and the attenuation length of laser λ in water is 400 μm. The microchamber dimensions given by Liu et al. are $L = 7$ mm, and $H = 240$ μm, which is sandwiched by a 1mm thick glass top slide and a 1mm thick sapphire bottom slide. The EVs have $d_p = 100$ nm, c=10^{-7} μL, $S_T = -0.03$ K^{-1} and $D = 4.4 \times 10^{-12} m^2 s^{-1}$. PS nanoparticles, each with a diameter of 100 nm, are used to represent EVs. The no slip boundary condition is employed at all walls in calculating the particle trajectories. The initial temperature is defined to be 25°C for the entire computational domain.

The coupled solutions of the flow field and heat transfer are first obtained using the FEM software. By trial and error, sufficient mesh resolution is guaranteed for attaining numerical convergence. Fig. 2 illustrates the temperature field ranging from 25°C to 57°C on the x-z plane. Laser irradiation heats up the middle part of the microchamber, and a cold region is formed on the chamber bottom beneath the heated core. Owing to the different heat capacities among water, glass and sapphire, the heated core takes up a complexed shape. Fig. 3 shows the velocity field with the magnitude ranging from 0 to 60 μm/s. A toroidal convection vortex is formed, which draws the near-bottom fluid to converge to the centre of the microchamber bottom and pushes the near-top fluid away from the centre of the microchamber. After obtaining the flow field and temperature distribution, the particle tracing module is used to calculate the accumulation process of the PS nanoparticles to the cold bottom region below the heating spot owing to the thermophoretic effect. As displayed in Fig. 4, a target cylinder centred at the final positions of nanoparticles is set up to facilitate analyses of nanoparticle accumulation. The target cylinder's diameter is 100 μm, and its height is 5 μm. When a particle moves into the target cylinder, it is regarded to have arrived at its designated position. Fig. 5 shows the 3D visualisations of the nanoparticle distributions at the beginning and at the end of the simulation. The middle section of the computational domain, with a radius of 1000 μm and height of 240 μm, is shown for effective visualisation. Nanoparticles on the left-hand side of Fig. 5, are randomly distributed in the chamber at 0 s. On the right-hand side of Fig. 5, after heating for 10 mins, nanoparticles have all entered the target cylinder at the centre of the chamber bottom and reached a steady state. The nanoparticles in the target cylinder are enriched from 1-fold to 1,400-fold. Because of the little difference between ρ and ρ_p, the resultant gravity and buoyancy forces are negligible compared to other forces. The influences of the thermophoretic forces and the drag forces are much more significant than other forces, so the nanoparticle movement is governed by the temperature gradient-induced thermophoresis and thermal convection. Overall, our simulation is in good agreement with both the numerical and the experimental results reported in the literature.

4.2. Sensitivity to microchamber height

The enrichment behaviour can be influenced by the microchamber height due to the changes in temperature distribution and thermal convection. To study this influence, the chamber height is varied in a range from 80 to 320 μm in the simulation, and the target cylinder remains the same as in Section 4.1. The percentage of particles moving in

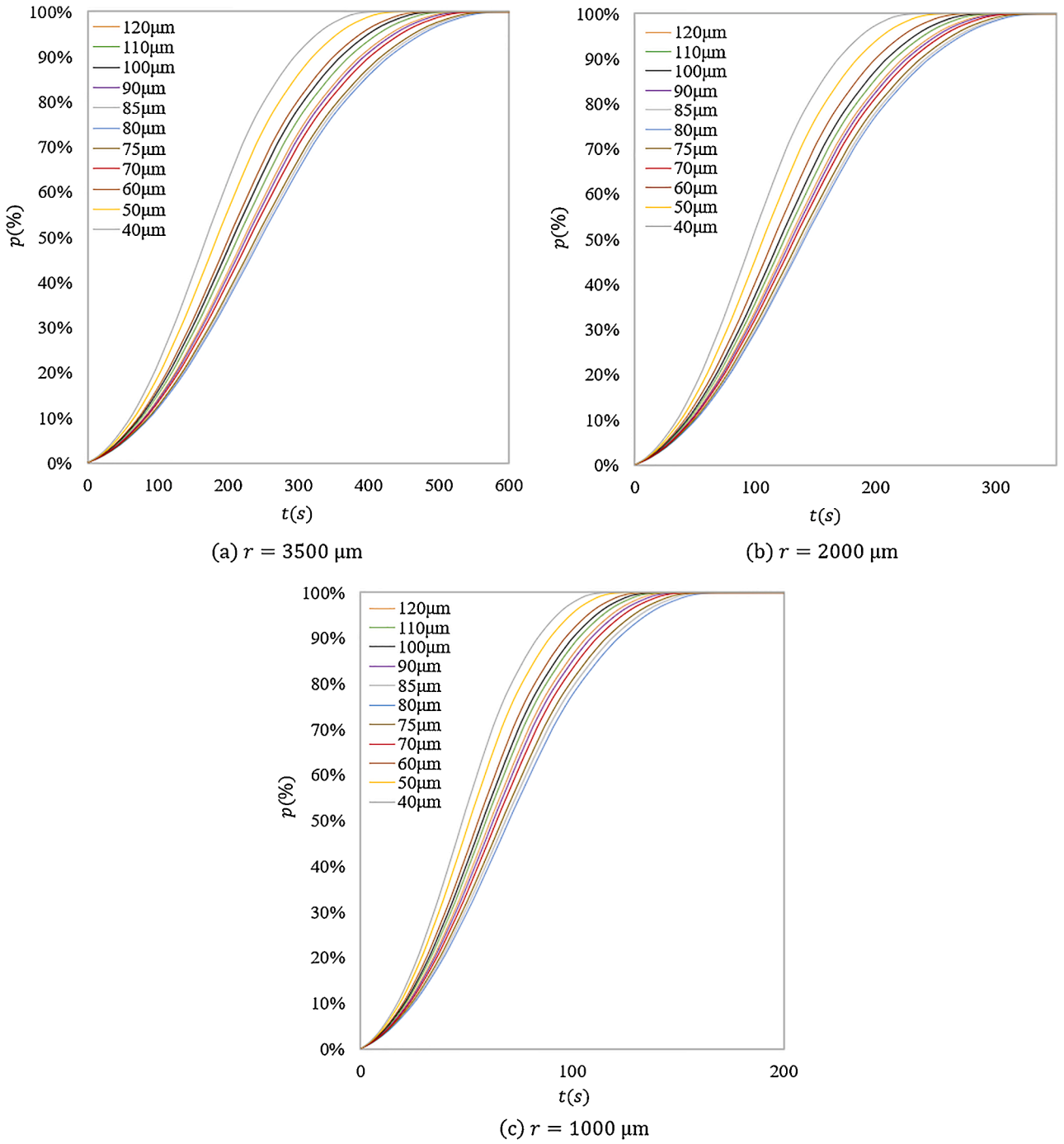

Fig. 14. Percentages of 100nm particles arriving at designated positions.

the target cylinder at a steady state is designated to be p^{∞}. If more than 99.5 % of particles move into the target cylinder at the steady state, then it is defined as an effective enrichment. A total of 20 heights are tested, but only three are illustrated in Fig. 6 to highlight the changes, i.e. $H =$ 80 μm, $H = 240$ μm and $H = 320$ μm. Fig. 6 (a–c) zooms in the target cylinder from the top, where the red circle represents the target cylinder boundary. When the height is 80 μm, nanoparticles remain randomly distributed in the microchamber, with only about 10 % of particles moving into the target cylinder. As the height of the microchamber increases, more particles move towards the target cylinder. When the height is equal to 238 μm, about 99.5 % of the particles move into the target cylinder, indicating an effective enrichment. Such good performance is kept until the height of 262 μm. Fewer particles move into the target cylinder and nanoparticles are dispersed over a larger region when the height gradually increases from 262 μm to 320 μm. Fig. 7 demonstrates the variations of the percentage of particles arriving at the targeted cylinder with time for representative chamber heights at a 40 μm interval. Fig. 8 shows how the final percentage of particles arriving at the target cylinder varies with all the channel heights, which indicates the optimum height range is between 238 μm and 262 μm. The chamber height $H = 240$ μm used in the literature lies in this range.

The mechanism behind the accumulation performance can be attributed to the competition between thermophoresis and thermal convection effects. Fig. 9 shows the temperature gradients (blue) and the convection flow speeds (orange) at a level 5 μm above the centre of the bottom of the microchamber. When the height is less than 160 μm, due

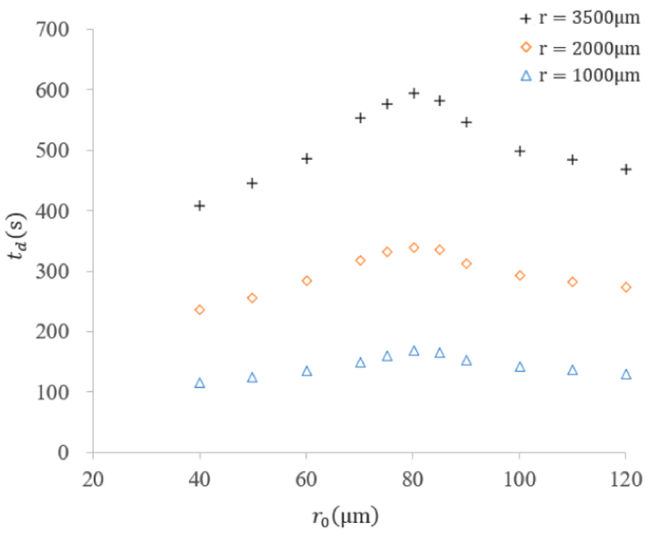

Fig. 15. Time of the nanoparticles reaching the final positions for all tested r_0 values.

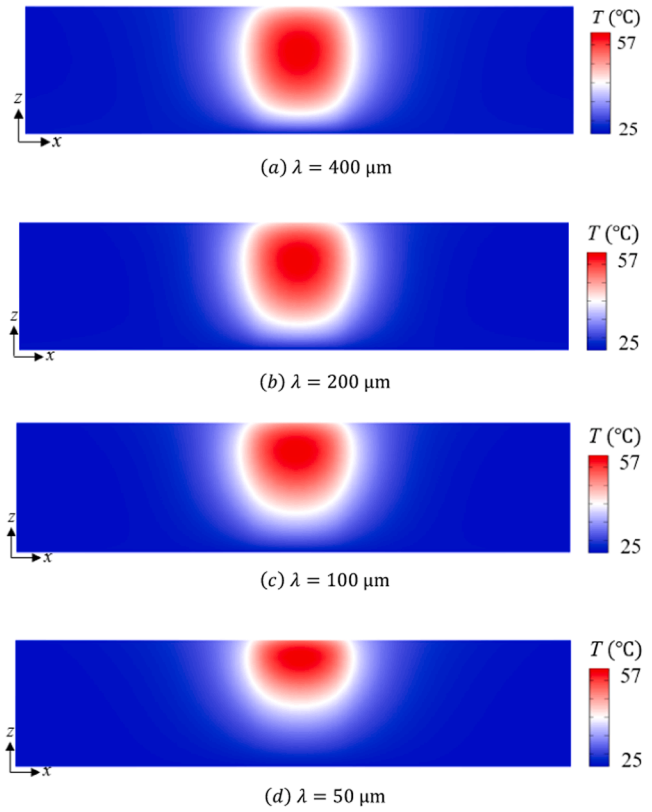

Fig. 16. Temperature fields of different λ values.

to the increase of both the temperature gradient and convection speed, the accumulation performance is gradually improved. When the height is between 160 μm and 262 μm, the magnitude of the temperature gradient is almost stabilised. Reasonable strength of the natural convection is necessary for transporting particles to the centre of the chamber's bottom boundary, just below the heated core, therefore facilitating the accumulation of particles. When the height exceeds 262 μm, the thermophoretic force gradually decreases while the drag force keeps increasing. The weakened temperature gradient leads to a smaller thermophoretic force, which will have difficulty to push downward the upwelling of the nanoparticles due to the convective current, resulting in a reduction of the thermophoretic efficiency.

5. Parametric studies

5.1. Influence of laser spot radius

This section uses the validated model to study the influence of the spot radius of the laser (r_0) on the thermophoretic accumulation of nanoparticles. A total of 15 radii are tested, ranging from 10 μm to 120 μm. The particle diameter is fixed at 100 nm. The tested radii of the microchamber (r) are 1000 μm, 2000 μm, and 3500 μm. To facilitate analyses in the calculation of nanoparticle accumulation, the target cylinder is set up that is just big enough to include all the particles at the steady state in each test. The time taken by the nanoparticles to reach the steady state is defined as t_d.

Fig. 10 illustrates the temperature fields of four representative r_0. The width of the heat core decreases with the decrease of r_0 from 120 μm to 40 μm. Fig. 11 demonstrates how the maximum temperature (T^*) increases from 39.8 °C to 397 °C when r_0 decreases from 120 μm to 10 μm, which is attributed to the increase in laser power density. When $r_0 < 40$ μm, the maximum temperature is more than 100 °C, therefore the liquid will boil and should not be considered here. When $r_0 \geq 40$ μm, nanoparticles can accumulate toward the centre of the chamber bottom. Fig. 12(a–c) show the close-up around the target cylinder from the top, where the orange circle, red circle and blue circle represent the target cylinders with radii of 50 μm, 100 μm and 150 μm, respectively. The nanoparticles are much more concentrated when $r_0 = 40$ μm, but they become more dispersed with the increase in r_0. As presented in Fig. 13, the radius of the target cylinder (r_1) is approximately 1.25 times r_0 for all tested cases. These results indicate that the final position of particles can be controlled by r_0. Fig. 14 (a–c) show the variation in the percentage of nanoparticles arriving at designated positions for all tested r_0 with three different chamber sizes r = 1000 μm, 2000 μm, and 3500 μm. Fig. 15 presents the time taken by all the nanoparticles to reach the target cylinder in three different-sized chambers r = 1000 μm, 2000 μm, and 3500 μm. For each r_0, t_d reduces with r, because at larger r corresponds to a more extensive distribution of nanoparticles at $t = 0$. The value of t_d depends on the thermophoretic strength and the size of the target cylinder. When $r_0 = 40$ μm, the thermophoretic process is strong and the nanoparticles move at a large speed. When r_0 increases from 40 μm to 80 μm, the thermophoretic force decreases rapidly, corresponding to the reduced temperature gradient, therefore the particle accumulation velocity reduces. Although the travelling distance of the particle is shortened due to the enlarged size of the target cylinder, t_d still increases as the particle velocity is reduced at a greater rate. When r_0 increases from 80 μm to 120 μm, the particle velocity slightly reduces as T^* decreases gradually. However, the travelling distance of the particle is continuously shortened with the enlarged size of the target cylinder, resulting in a decrease of t_d. Based on the above argument, the optimum r_0 can be determined based on the maximum temperature tolerance of the live particles and the required concentration area.

5.2. Influence of light attenuation length in liquid

This section investigates the influence of the attenuation length of the laser in fluid on the thermophoretic accumulation of the nanoparticles. The tested attenuation length of the laser in fluid (λ) ranges from 50 μm to 500 μm, the particle diameter is fixed at 100 nm, and the tested radius of the microchamber (r) is 3500 μm. The target cylinder is specified to be 100 μm in diameter and 5 μm in height, which has the same dimensions as the experiment in Liu et al. [10]. In this study, we regard the enrichment to be effective if more than 99.5 % of particles move into the target cylinder.

As seen in Fig. 16, the temperature fields with four different λ are chosen, from a total of seven tests, to demonstrate the influence of the

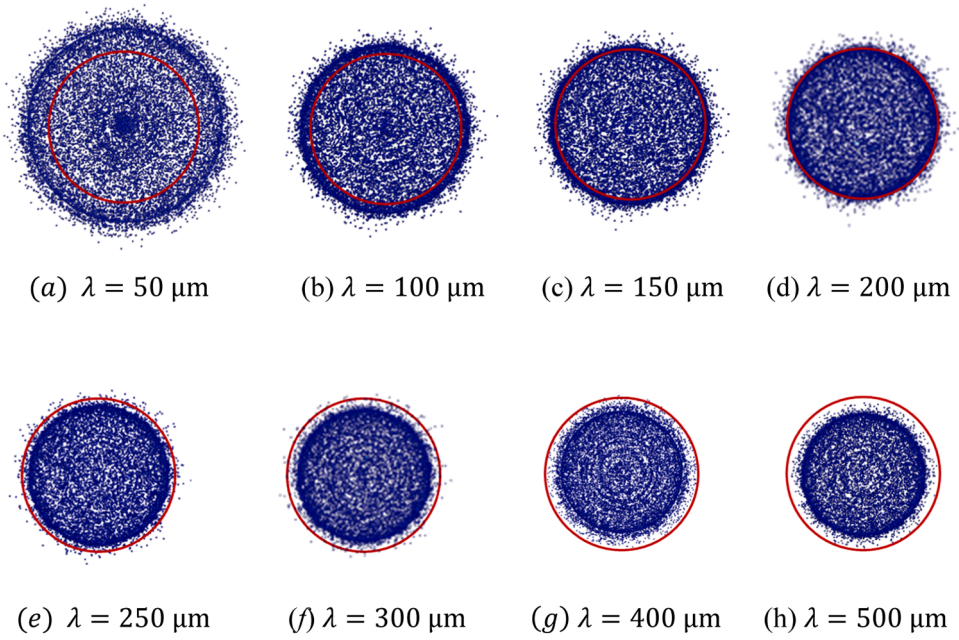

Fig. 17. Top view of target cylinder at the steady state for different λ values.

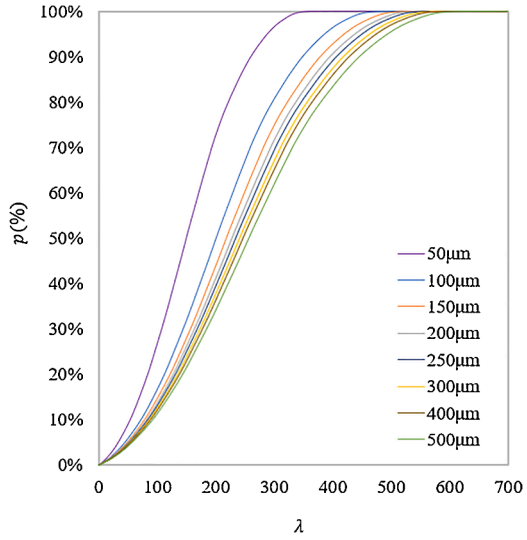

Fig. 18. Percentages of 100nm particles arriving at designated positions (r = 3500 μm).

attenuation length. When λ decreases from 500 μm to 50 μm, the gap between the heating core and the bottom of the chamber gradually increases. In all the tests, nanoparticles can accumulate towards the centre of the cold chamber bottom and reach a steady state. Fig. 17 (a–h) zoom in around the target cylinder in a plan view, where the red circle represents the target cylinder boundary. It is found that the particles become more concentrated when λ is increased from 50 μm to 500 μm. Fig. 18 shows the variation of the percentage of nanoparticles arriving at designated positions with time. The results show that the value of λ correlates positively to the time taken by nanoparticles to arrive at their final positions. With the increase of λ, the gap between the heating core and the chamber bottom decreases, strengthening the thermophoretic effect near the bottom of the chamber and therefore reducing the area of the final nanoparticle distribution. The reduced accumulation area leads to longer travelling distances of particles from the initial to final positions, resulting in an increase in accumulation time. Fig. 19 shows that

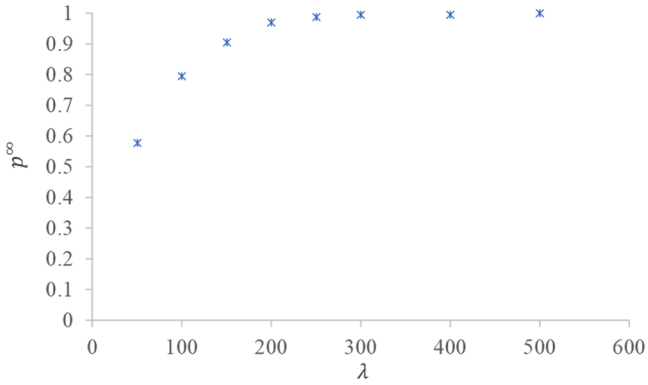

Fig. 19. Final percentages of particles in the target cylinder for all tested λ values.

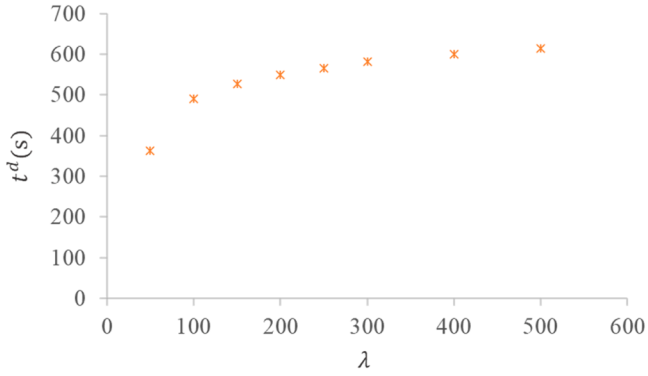

Fig. 20. Time of the nanoparticles reaching the final positions for all tested λ values.

p^{∞} increases with λ, and the effective enrichment is achieved when λ is greater than 250 μm. As shown in Fig. 20, t_d continuously increases from approximately 362 s to 620 s when λ increases from 50 μm to 500 μm. This indicates that there is an optimum λ between 250 μm and 300 μm,

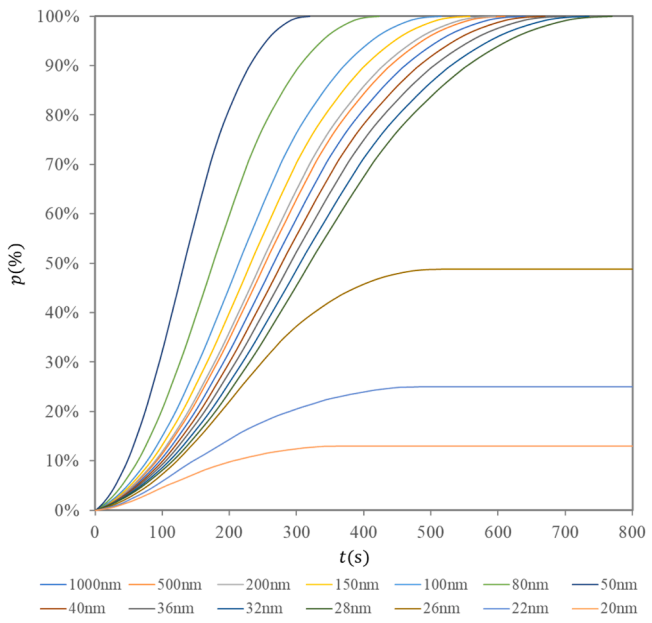

Fig. 21. Variation of the percentages of particles in the target cylinder and its sensitivity to particle diameter.

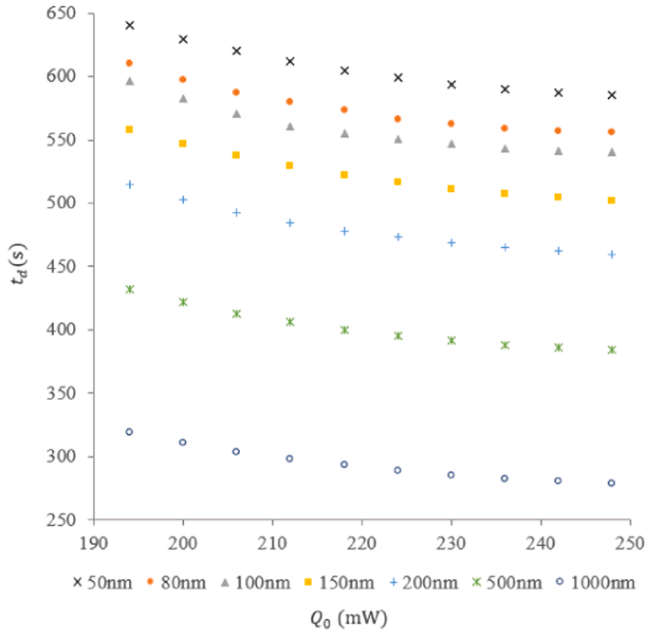

Fig. 22. Influences of Q_0 on t_d for different particle sizes.

which can achieve effective enrichment with minimum t_d. Compared to the value of $\lambda = 400$ μm used in the literature, the optimum λ could reduce the accumulation time of nanoparticles by about 6 %.

5.3. Influence of particle size

This section determines the influence of the particle size on the motion of suspended particles. A total of 14 sizes of polystyrene particles are examined, with the diameter ranging from 20 nm to 1000 nm. The target cylinder, t_d, p^∞ and optimum enrichment are defined to be the same as those in Section 5.2. The tested radius of the microchamber is 3500 μm. Fig. 21 demonstrates the variation of the percentage of particles reaching the target cylinder with time. It shows that the critical particle radius is about 28 nm with the current setup. For particles whose d_p are less than the threshold value, the thermophoretic effect is small and their movements are dominated by thermal convection. Some particles slowly circulate within the streaming vortices, but they cannot rest in the target cylinder, therefore effective enrichment cannot be achieved. When d_p exceeds the threshold size, the movement of particles is mainly governed by the thermophoretic force. Particles are increasingly concentrated in the target cylinder, and eventually achieve effective enrichment. The speed of the particle accumulation is clearly seen to correlate positively with the particle size.

5.4. Influence of laser power

Using the validated model, this section studies the influence of the laser power (Q_0) on the enrichment of the nanoparticles. The tested Q_0 ranges from 194 mW to 248 mW, and the test is conducted at intervals of 6 mW. With the increase of Q_0, the maximum temperature increases from 57 °C to 66°C. The tested nanoparticle diameters range from 50 nm to 1000 nm, and the target cylinder, t_d, and the optimum enrichment criterion are defined in the same way as those in Section 5.2. Fig. 22 demonstrates the arrival time required for effective enrichment of all the tested powers. For all the tested particle sizes, with the increase of laser power, the arrival time of all the tested nanoparticles gradually reduced. For example, with the increase of laser power by 54 mW, consequently increasing the temperature by 9°C, the arrival time of nanoparticles is reduced by approximately 60 s. This is because the thermophoretic force exerted on the particles is proportional to the temperature gradient. The larger the laser power, the larger the temperature gradient, and thus the larger the accumulating velocity.

6. Conclusions

A FEM model has been established to study the thermophoretic accumulation of nanoparticles. An IR laser is used to generate the temperature gradient within the fluid/particle mixture in a microchamber, which is sandwiched by a glass top and a sapphire bottom. The motion of the particles is determined by the thermophoretic force, induced by temperature gradient, and the drag and lift forces, induced by thermal convection. The model is verified against an experiment reported in the literature. It is found that the optimum microchamber height ranges from 238 μm to 262 μm. The microchamber height used in the past experiment is within this optimum height range.

The numerical model is first used to study the influence of the laser spot radius (r_0). For different microchamber radii, the radius of the accumulation zone, which encompasses all the particles at the steady state, is approximately 1.25 times the spot radius of the laser beam. The time taken by the nanoparticles to reach the steady state (t_d) increases with the microchamber radius. When r_0 increases from 40 nm to 80 nm, t_d increases with r_0. After reaching the peak value at 80 nm, it decreases with a further increase of r_0 from 80 nm to 120 nm.

The influence of the attenuation length of laser (λ) is then investigated. The results show that the particles at the final designated positions become more concentrated when λ increases. Effective enrichment, corresponding to more than 99.5 % of particles moving into the target cylinder, is achieved when λ is greater than 250 μm. It is also found that t_d increases with the increase of λ. The optimum value of λ is between 250 μm and 300 μm with current setup.

The influence of the nanoparticle size on the particle enrichment is then studied. With the current setup, the threshold diameter is found to be 28 nm. The speed of the particle enrichment increases with the particle size. Moreover, the influence of the laser power on the enrichment of nanoparticles is also studied. As expected, an increase of laser power reduces the time taken by the nanoparticles to reach the steady state.

CRediT authorship contribution statement

Jing Dong: Conceptualization, Writing – original draft, Writing – review & editing, Validation, Investigation, Methodology, Project administration. **Dongfang Liang:** Conceptualization, Writing – review & editing, Methodology, Project administration, Supervision. **Xinan Chen:** Writing – review & editing. **Xin Yang:** Conceptualization, Resources.

Declaration of Competing Interest

The authors declare that they have no known competing financial interests or personal relationships that could have appeared to influence the work reported in this paper.

Data availability

No data was used for the research described in the article.

Acknowledgements

The work has been supported by the Energy IRC Small Grants scheme funded by the Isaac Newton Trust/ Energy Policy Research Group (EPRG) and the NERC Discipline Hopping for Environmental Solutions initiative. We would like to thank Professor Weihong Tan at Hunan University, Professors Jiashu Sun and Chao Liu at National Center for Nanoscience and Technology (NCNST) for providing help in our model verification. For the purpose of open access, the authors have applied a Creative Commons Attribution (CC BY) licence to any Author Accepted Manuscript version arising from this submission.

References

[1] L.M. Doyle, M.Z. Wang, Overview of extracellular vesicles, their origin, composition, purpose, and methods for exosome isolation and analysis, Cells 8 (2019).
[2] R. Spaull, B. McPherson, A. Gialeli, A. Clayton, J. Uney, A. Heep, Ó. Cordero-Llana, Exosomes populate the cerebrospinal fluid of preterm infants with post-haemorrhagic hydrocephalus, Int. J. Dev. Neurosci. 73 (2019) 59–65.
[3] Y.K. Cho, J.G. Lee, J.M. Park, B.S. Lee, Y. Lee, C. Ko, One-step pathogen specific DNA extraction from whole blood on a centrifugal microfluidic device, Lab Chip 7 (2007) 565–573.
[4] J. Zhang, Q. Guo, M. Liu, J. Yang, A lab-on-CD prototype for high-speed blood separation, J. Micromech. Microeng. 18 (2008).
[5] D. Di Carlo, D. Irimia, R.G. Tompkins, M. Toner, Continuous inertial focusing, ordering, and separation of particles in microchannels, Proc. Natl. Acad. Sci. U. S. A. 104 (2007) 18892–18897.
[6] A.T. Kadaksham, P. Singh, N. Aubry, Dielectrophoresis of nanoparticles, Electrophoresis 25 (2004) 3625–3632.
[7] K.C. Neuman, S.M. Block, Optical trapping, Rev. Sci. Instrum. 75 (2004) 2787–2809.
[8] J. Dong, D. Liang, X. Yang, C. Sun, Influences of microparticle radius and microchannel height on SSAW-based acoustophoretic aggregation, Ultrasonics 117 (2021), 106547.
[9] S. Maramizonouz, X. Tao, M. Rahmati, C. Jia, R. Tao, H. Torun, T. Zheng, H. Jin, S. Dong, J. Luo, Y. Fu, Flexible and bendable acoustofluidics for particle and cell patterning, Int. J. Mech. Sci. 202-203 (2021), 106536.
[10] C. Liu, J. Zhao, F. Tian, L. Cai, W. Zhang, Q. Feng, J. Chang, F. Wan, Y. Yang, B. Dai, Y. Cong, B. Ding, J. Sun, W. Tan, Low-cost thermophoretic profiling of extracellular-vesicle surface proteins for the early detection and classification of cancers, Nat. Biomed. Eng. 3 (2019) 183–193.
[11] F. Tian, S. Zhang, C. Liu, Z. Han, Y. Liu, J. Deng, Y. Li, X. Wu, L. Cai, L. Qin, Q. Chen, Y. Yuan, Y. Liu, Y. Cong, B. Ding, Z. Jiang, J. Sun, Protein analysis of extracellular vesicles to monitor and predict therapeutic response in metastatic breast cancer, Nat. Commun. 12 (2021) 2536.
[12] C. Ludwig, Diffusion zwischen ungleich erwärmten Orten gleich zusammengesetzter Lösungen, Enthalten in Sitzungsberichte der mathematisch-naturwissenschaftlichen Classe der Kaiserlichen Akademie der Wissenschaften Wien, Aus der K.K. Hof Staatsdruckerei 65 (1856) 539.
[13] S. Rashidi, F. Hormozi, N. Karimi, W. Ahmed, Applications of nanofluids in thermal energy transport, Emerg. Nanotechnol. Renew. Energy (2021) 345–368.
[14] S. Ramachandran, C.B. Sobhan, G.P. Peterson, Thermophoresis of nanoparticles in liquids, Int. J. Heat Mass Transf. 147 (2020), 118925.
[15] P. Blanco, M.M. Bou-Ali, J.K. Platten, D.A. de Mezquia, J.A. Madariaga, C. Santamaria, Thermodiffusion coefficients of binary and ternary hydrocarbon mixtures, J. Chem. Phys. 132 (2010), 114506.
[16] D. Braun, A. Libchaber, Trapping of DNA by thermophoretic depletion and convection, Phys. Rev. Lett. 89 (2002), 188103.
[17] M. Huang, J. Yang, T. Wang, J. Song, J. Xia, L. Wu, W. Wang, Q. Wu, Z. Zhu, Y. Song, C. Yang, Homogeneous, low-volume, efficient, and sensitive quantitation of circulating exosomal PD-L1 for cancer diagnosis and immunotherapy response prediction, Angew. Chem. Int. Ed. Engl. 59 (2020) 4800–4805.
[18] Y.T. Maeda, T. Tlusty, A. Libchaber, Effects of long DNA folding and small RNA stem-loop in thermophoresis, Proc. Natl. Acad. Sci. U. S. A. 109 (2012) 17972–17977.
[19] A. Errarte, A. Martin-Mayor, M. Aginagalde, I. Iloro, E. Gonzalez, J.M. Falcon-Perez, F. Elortza, M.M. Bou-Ali, Thermophoresis as a technique for separation of nanoparticle species in microfluidic devices, Int. J. Therm. Sci. 156 (2020).
[20] A. Sanjuan, A. Errarte, M.M. Bou-Ali, Analysis of thermophoresis for separation of polystyrene microparticles in microfluidic devices, Int. J. Heat Mass Transf. 189 (2022), 122690.
[21] C. Zhao, J. Fu, A. Oztekin, X. Cheng, Measuring the Soret coefficient of nanoparticles in a dilute suspension, J. Nanopart. Res. 16 (2014) 2625.
[22] D.A. Drew, Mathematical modeling of two-phase flow, Annu. Rev. Fluid Mech. 15 (1983) 261–291.
[23] A.A. Minea, Advances in Industrial Heat Transfer, CRC Press, 2013.
[24] J.L. Anderson, Colloid transport by interfacial forces, Annu. Rev. Fluid Mech. 21 (1989) 61–99.
[25] W. Li, E.J. Davis, Measurement of the thermophoretic force by electrodynamic levitation: microspheres in air, J. Aerosol Sci. 26 (1995) 1063–1083.
[26] R. Wang, S. Sun, W. Wang, Z. Zhu, Investigation on the thermophoretic sorting for submicroparticles in a sorter with expansion-contraction microchannel, Int. J. Heat Mass Transf. 133 (2019) 912–919.
[27] A. Guha, Transport and deposition of particles in turbulent and laminar flow, Annu. Rev. Fluid Mech. 40 (2008) 311–341.
[28] P.G. Saffman, The lift on a small sphere in a slow shear flow, J. Fluid Mech. 22 (2006) 385–400.
[29] R. Clift, J.R. Grace, M.E. Weber, Bubbles, Drops, and Particles, Dover Publications, Incorporated, 2013.
[30] M.M. Kim, A.L. Zydney, Effect of electrostatic, hydrodynamic, and Brownian forces on particle trajectories and sieving in normal flow filtration, J. Colloid Interface Sci. 269 (2004) 425–431.
[31] E. Michaelides, Brownian movement and thermophoresis of nanoparticles in liquids, Int. J. Heat Mass Transf. 81 (2015) 179–187.
[32] A. Li, G. Ahmadi, Dispersion and deposition of spherical particles from point sources in a turbulent channel flow, Aerosol. Sci. Technol. 16 (4) (1992) 209–226.